

Accuracy Limits for Globally-Referenced Digital Mapping Using Standard GNSS

Lakshay Narula¹, Matthew J. Murrian², and Todd E. Humphreys²

Abstract—Exchange of location and sensor data among connected and automated vehicles will demand accurate global referencing of the digital maps currently being developed to aid positioning for automated driving. This paper explores the limit of such maps' globally-referenced position accuracy when the mapping agents are equipped with low-cost Global Navigation Satellite System (GNSS) receivers performing standard code-phase-based navigation. The key accuracy-limiting factor is shown to be the asymptotic average of the error sources that impair standard GNSS positioning. Asymptotic statistics of each GNSS error source are analyzed through both simulation and empirical data to show that sub-50-cm accurate digital mapping is feasible in moderately urban environments in the horizontal plane after multiple mapping sessions with standard GNSS, but larger biases persist in the vertical direction.

I. INTRODUCTION & MOTIVATION

Localization is one of the primary operations that connected and automated vehicles must perform, both to navigate from one location to another and to interact with each other and with their surroundings within a mapped environment. Satellite-based navigation sensors have historically been the unrivalled sensor of choice for navigating from source to destination. However, the high-reliability sub-50-cm precision demanded by automated vehicles for lane-keeping and other applications, especially in urban areas, has significantly changed this landscape [1]. In most automated vehicles being developed, the GPS/GNSS receiver is relegated to a secondary sensor whose role is to loosely constrain (within a few meters) the primary localization sensors, usually camera(s) and/or LiDAR, to a global reference frame when building a digital map. The vehicles then locate themselves to decimeter accuracy within this digital map.

Automated driving does not necessarily demand sub-50-cm agreement between the coordinates of a given point in the digital map and the coordinates of the same point in a well-defined global reference frame. Rather, local self-consistency and accurate localization within the digital map is of greater importance. However, consistency of the digital map with a global coordinate frame is likely to become a pre-requisite for cooperative automated driving. If all collaborating vehicles navigate within the same digital map, then precise exchange of information such as vehicle position, velocity, intent, etc. is possible [2], [3], even if the map itself is only globally accurate to a few meters. However, it is unlikely that automated vehicles from different manufacturers will

rely on a common digital map. Consequently, the accuracy of the exchanged vehicle position is lower-bounded by the disagreement on the coordinates of the same physical location between different maps. Thus, exchange of accurate vehicle pose among vehicles, as well as other associated high-level information such as sensor data in the vehicle's body frame, will demand consistency among, or translation between, different digital maps.

Standard code-phase-based GNSS position measurements, such as those provided by all mass-market GNSS receivers, may be biased by as much as 3–5 meters on any given mapping session. Maps anchored by these measurements may not exhibit lane-level consistency with each other. One possible solution is to create digital maps with decimeter-accurate carrier-phase differential GNSS (CDGNSS) systems [4]. However, at current prices, such systems can only be installed on a limited fleet of specialized mapping vehicles. Precise point positioning (PPP) techniques offer a low-cost alternative to CDGNSS, but the frequent cycle-slipping experienced in urban areas impedes the convergence of PPP techniques [5].

This paper explores the accuracy limit of globally-referenced mapping involving collaborating consumer vehicles whose sense of global position is based on standard code-phase-based GNSS receivers. Key parameters in this exploration are the asymptotic averages of the error sources that impair code-phase-based GNSS positioning: receiver thermal noise, satellite clock and orbit errors, ionospheric and tropospheric modeling errors, and multipath. One or more vehicles navigating through a digital map over time make multiple time-separated GNSS measurements of the same location. If these vehicles collaboratively update the map over multiple sessions, then the GNSS errors are averaged across all sessions with appropriate weighting.

Are the GNSS errors at every map location—including deep urban locations—asymptotically zero-mean, or, on the contrary, do location-dependent biases persist in averages of time-separated standard GNSS measurements? Such is the question this paper seeks to address.

II. PREVIOUS WORK

Improving the accuracy of maps by averaging GPS/GNSS tracks has been explored previously using a variety of approaches. An early effort, detailed in [6], proposed the precise determination of lane centerlines by clustering and averaging the GNSS tracks of probe vehicles. The accuracy of the estimated centerline was assessed in terms of the spread of GNSS tracks, assuming, without analysis, that the

¹Department of Electrical and Computer Engineering, The University of Texas at Austin, Austin, TX 78712, USA

²Department of Aerospace Engineering and Engineering Mechanics, The University of Texas at Austin, Austin, TX 78712, USA

error was zero-mean at every location. More recently, [7] proposed vehicle lane determination via PPP on a rural road under open-sky conditions. The current paper aims to perform localization at a similar accuracy level, but in urban and suburban areas and with the aid of a digital mapping sensor.

Minimizing the difference between GNSS measurements and the assigned map coordinates of locations visited multiple times by probe vehicles has been a common feature of the seminal works on map-based precise localization in urban environments for automated driving [2], [3], but no analysis of the accuracy of the resulting map in the global coordinate system was provided.

The effect of multipath on measured pseudoranges was studied extensively for various signal types in [8]. However, this study was done under open-sky conditions with a static survey-grade antenna, hardly representative of a mass-market receiver in an urban environment. A detailed study on the distribution of code-phase and Doppler offsets of the multipath components from individual satellites in a dynamic urban setting was carried out in [9]. However, the error was characterized as the combined distribution of code phase delays over the entire duration of the run, which marginalizes over the temporally- and physically-local biases. On the contrary, this paper explores the errors in the position domain for repeated sessions through a given realization of an urban corridor.

Other GNSS error sources such as errors in modeling of ionospheric [10] and tropospheric [11] delay have been studied extensively over many decades, and their long-term error characteristics have also been reported in the literature. However, the impact of these errors on the asymptotic statistics of code-phase-based GNSS position estimates has not been previously presented.

To the authors' best knowledge, despite the apparent simplicity of the problem, no prior work has studied the long-term statistics of GNSS errors in an urban environment representative of the conditions to be encountered by consumer vehicles creating digital maps.

Note that an extended version of this paper, submitted for review after an initial version of this paper was accepted for the ITSC, has been published in [12]. The current paper corrects a few typographical errors in the extended version.

III. GNSS ERROR ANALYSIS

A. Low-Cost GNSS in Urban Areas

Low-cost multi-GNSS receiver manufacturers have recently announced the development and release of low-cost multi-frequency multi-GNSS receivers. Accordingly, the analysis in this section considers a vehicular platform equipped with a multi-frequency multi-GNSS receiver capable of tracking both code and carrier phase of GNSS signals.

Development of an extensive dense reference network in support of CDGNSS consumer vehicular positioning in urban areas, as suggested in [13], could be an expensive affair. PPP is a low-cost alternative to CDGNSS that requires only a sparse network of reference stations across the globe, but is

not considered a viable option for urban GNSS positioning in this paper because the constant cycle slips and outages experienced in urban areas [4] make it difficult for PPP's float carrier phase ambiguity estimates to converge [5], in which case PPP degrades to code-phase positioning accuracy.

While convergence of PPP carrier-phase ambiguities may be infeasible in urban areas, a partial PPP solution that exploits precise satellite orbits and clocks, as well as ionospheric and tropospheric corrections, can certainly improve the accuracy of code-phase-based GNSS position estimates. Since connected and automated vehicles will perform enjoy network connectivity, this paper assumes the availability of such GNSS corrections. Thus, the kind of GNSS errors assessed in this section lie between those corresponding to the two extremes of standard standalone code-phase positioning and PPP. This type of GNSS positioning, hereafter referred to as enhanced code-phase positioning, exploits both code and carrier phase or frequency tracking, but, as opposed to PPP, does not attempt to estimate a quasi-constant float carrier phase ambiguity, making it suitable for urban applications.

B. Pseudorange Measurement

The nonlinear pseudorange measurement vector $\rho \in \mathbb{R}^{n_z}$ from n_z satellites is linearized around an initial estimate of the receiver state \bar{x} , modeled ionospheric delay \bar{I} , and modeled tropospheric delay \bar{T} as

$$\rho = \mathbf{h}(\bar{x}, \bar{I}, \bar{T}) + H(\mathbf{x} - \bar{x}) + \tilde{I} + \tilde{T} + \mathbf{w}. \quad (1)$$

where \mathbf{h} denotes the nonlinear measurement model vector, H denotes the Jacobian of the measurement model evaluated at \bar{x} , \mathbf{x} denotes the true state of the receiver, and $\tilde{I} \triangleq I - \bar{I}$, $\tilde{T} \triangleq T - \bar{T}$ with I and T denoting the true ionospheric group delay and tropospheric delay, respectively. The measurement noise \mathbf{w} denotes the sum of measurement thermal noise, multipath interference, non-line-of-sight (NLOS) delay, and other unmodeled errors.

Rearranging measured and modeled quantities on the left-hand side to get the standard form for a linearized measurement model yields

$$\mathbf{z} \triangleq \rho - \mathbf{h}(\bar{x}, \bar{I}, \bar{T}) + H\bar{x} = H\mathbf{x} + \tilde{I} + \tilde{T} + \mathbf{w}. \quad (2)$$

By solving (2) for \mathbf{x} , updating \bar{x} , and iterating until convergence, the receiver estimates its position and clock bias. For dynamic applications such as vehicle tracking, the state \mathbf{x} is typically augmented to include the time derivatives of receiver position and clock bias, and the measurement model typically assumes direct measurement of apparent Doppler frequency.

C. Error Sources

The major sources of error in the estimated receiver state are as follows:

1) *Thermal Noise*: Measurement thermal noise at the receiver is one of the components of \mathbf{w} in (1). The effect of thermal noise can be accurately modeled as a white Gaussian random variable with zero mean and standard deviation σ_T . For the pseudorange measurement, σ_T is typically between

10–30 cm, depending on the signal carrier-to-noise ratio, signal bandwidth, and receiver tracking bandwidth [14]. Estimation of the receiver state from multiple appropriately-weighted measurements with independent thermal-noise errors, and processing such measurements over time through a filter based on the modeled dynamics of the receiver, renders negligible the position-domain effects of uncorrelated zero-mean thermal noise. As a result, thermal noise is not a major contributor to the asymptotic accuracy of a digital map.

2) *Satellite Orbit and Clock Errors*: Satellite orbit and clock errors manifest in the modeled satellite position and the modeled satellite clock bias. The International GNSS Service (IGS) provides orbit and clock models for GNSS satellites. The 17-h retroactively-available *rapid* orbits and satellite clock models are accurate to ~ 2.5 cm and ~ 75 ps RMS errors, respectively [15], adding up to less than 5 cm of RMS error in the modeled pseudorange for a given signal. Since the orbit and clock parameters are fit to measurements made at IGS analysis centers, the errors in the estimated parameters must be asymptotically zero-mean by design of the estimator. For post-processing applications such as mapping, it is reasonable to assume the availability of *rapid* orbit and satellite clock products, and thus the asymptotic average position errors due to errors in modeled satellite position and clock bias can be reduced to a sub-5-cm level.

3) *Ionospheric Modeling Errors*: The ionospheric delay of GNSS signals can be estimated via an ionosphere model or, in case of a multi-frequency receiver, eliminated via a combination of multiple-frequency pseudorange measurements. The latter technique does not require any external aiding, but the formation of the ionosphere-free combination exacerbates pseudorange noise, including any biases due to tracking of multipath signals. While both methods have their merits, the analysis in this section considers corrections from an ionospheric model, and thus will not be relevant to applications where the ionosphere-free combination is applied. Note that those applications would likely experience worse multipath errors than the ones presented later, requiring a separate multipath analysis along the lines of Section III-C.5.

Ionospheric model accuracy was studied comprehensively in [10]. The method in [10] generates unambiguous carrier-phase measurements from a global distribution of permanent receivers to compute the true slant total electronic content (STEC) for each satellite, and compares the model prediction for a number of models with the ground truth. This section extends the analysis in [10] to examine whether there exist long-term position-domain biases in enhanced code-phase positioning.

To observe the position-domain effect of the ionospheric modeling errors in isolation, this section neglects all other error sources, reducing the linearized measurement model in (2) to

$$z = Hx + \tilde{I}.$$

The post-fit residuals for multiple regional and global ionospheric models, computed as described in [10], were

graciously made available by the same authors for the year 2014. Historical GPS satellite almanacs can be combined with the timestamps from the residuals data to obtain the measurement sensitivity matrix H at each epoch for each station. With an elevation-dependent measurement covariance matrix R , the error in the weighted least-squares solution due to errors in ionospheric modeling is

$$\hat{x} - x = (H^T R^{-1} H)^{-1} H^T R^{-1} \tilde{I}.$$

Table I presents a numerical summary of the long-term average position error when applying ionospheric corrections from the IGS global ionospheric map (GIM), as estimated over 12 months of data from 2014 (more than 800,000 samples per station). Interestingly, there is clear evidence of a southward bias in the position error for stations in the northern hemisphere, and a northward bias in the position error for stations in the southern hemisphere. Results from a similar analysis for the Wide Area Augmentation System (WAAS) ionospheric corrections available for the contiguous United States (CONUS) region are also presented in Table I. The WAAS model was found to exhibit a significantly smaller RMS error in ionosphere TEC estimates when compared to the IGS GIM; however the long-term position bias due to WAAS corrections is similar to or worse than those for the IGS model.

TABLE I
LONG-TERM AVERAGE POSITION ERROR DUE TO IONOSPHERIC MODEL ERRORS (ϕ DENOTES STATION LATITUDE).

Ionosphere Model	Region	East (m)	North (m)
IGS	$\phi \geq 30^\circ$	0.0107	-0.2129
	$30^\circ > \phi > -30^\circ$	-0.0651	-0.0692
	$\phi \leq -30^\circ$	0.0237	0.2450
WAAS	CONUS	-0.0048	-0.2916
Fast PPP IONEX	$\phi \geq 30^\circ$	-0.0042	-0.0099
	$30^\circ > \phi > -30^\circ$	-0.0390	0.0013
	$\phi \leq -30^\circ$	-0.0325	-0.0087

Another global ionospheric model, the Fast PPP IONEX model [16], was also studied as above. In comparison with the IGS corrections, it is clear that the Fast PPP IONEX GIM corrections result in substantially unbiased long-term position errors at the global test locations. However, it must be conceded that the results in Table I are best-case results, as they are based on data from the same permanent reference stations used to constrain the model.

To understand the reason behind the systematic biases with IGS corrections, note that any ionospheric modeling bias that identically affects all satellites does not have any impact on the accuracy of the GNSS position solution, as this common error is absorbed in the clock bias estimate. Rather, position-domain biases arise from the azimuthal- and elevation-dependence of ionosphere model errors. From analysis of the spatial distribution of post-fit residuals, it was found that appreciable azimuthal and elevation residual gradients persist in the IGS ionospheric corrections. These

gradients are represented graphically in Fig. 1 for one representative station from the northern hemisphere (station code: EUSK, latitude: $50^{\circ}40'26.87''$, longitude: $6^{\circ}45'48.72''$) and one representative station from the southern hemisphere (station code: VACS, latitude: $-20^{\circ}17'48.47''$, longitude: $57^{\circ}29'13.79''$). The post-fit residuals are binned in azimuth and elevation and the average value in each bin is denoted by the color of the representing disc. The size of the disc denotes the number of samples of post-fit residuals available in each bin. Due to the inclination angle of the GPS satellite orbits, the angular distribution of satellites at any given latitude is non-uniform.

From Fig. 1, it is clear that the elevation gradients in the ionospheric residuals are pronounced. A subtle azimuthal gradient also exists, mainly along the north-south direction. Such spatial non-uniformity, coupled with the non-uniform satellite angular distribution, may be the reason for the observed persistent position biases. While the elevation gradients are consistent for stations at all locations, the azimuthal gradients appear to invert along the north-south direction between the northern and southern hemisphere. This is likely the reason for the opposite direction of the average horizontal position bias in the northern and southern hemispheres.

In conclusion, persistent decimeter-level biases in the east-north plane and meter-level biases in the vertical direction can arise when ionospheric delay corrections are sourced from the IGS GIM, or similar, even under ideal open-sky conditions. More advanced models of the ionosphere with more accurate slant TEC measurements may achieve better results. Elimination of the ionospheric delay based on the ionosphere-free combination is another option, but tends to worsen multipath-induced position errors. If corrections from some ionosphere model lead to unbiased position errors, then for globally-referencing digital maps by averaging GNSS measurements over many sessions it is advisable to avoid the combination of multi-frequency signals.

4) *Tropospheric Modeling Errors*: The tropospheric delay is obtained from models of the climatological parameters (temperature, pressure, and water vapor pressure) along the propagation path. State-of-the-art tropospheric models [11] fit a small number of location- and day-of-year-dependent coefficients to climatological data from numerical weather models (NWMs) to estimate the zenith delay, and subsequently apply a mapping function to map the zenith delay to a given zenith angle. For empirically-derived mapping functions such as Vienna Mapping Function (VMF1) [17] and Global Mapping Function (GMF) [18], the mean error at lowest elevation of 5° has been shown to be under 50 mm. As a result, this paper assumes that time-averaged tropospheric model errors would introduce sub-5-cm errors in the position domain, and would thus not impede asymptotically accurate collaborative mapping in both horizontal and vertical components at the several-decimeters level.

5) *Multipath Error*: In ideal circumstances, each signal received from an overhead satellite arrives only along the least-time path. In practice, however, this so-called line-

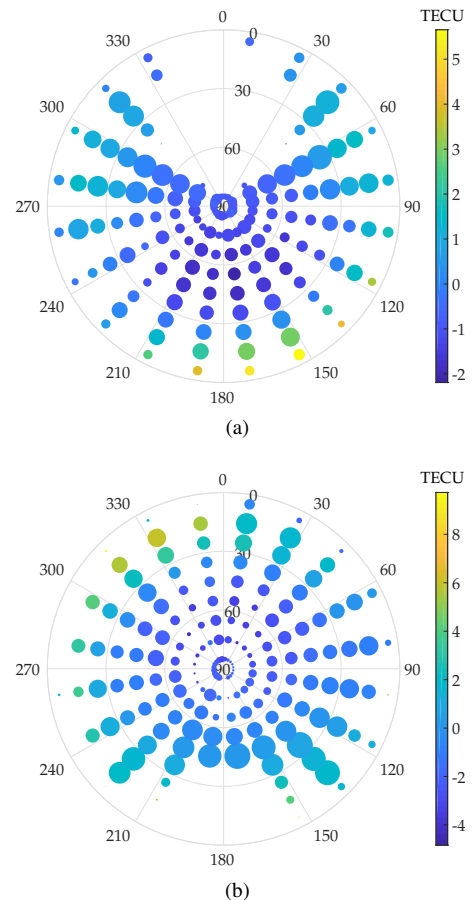


Fig. 1. Azimuth and elevation dependence of post-fit IGS GIM residuals. (a) A representative station from the northern hemisphere. (b) A representative station from the southern hemisphere. The average residual error, in total electron content (TECU), is denoted by the color of the disc. The size of the disc indicates the number of samples of post-fit residuals available in each bin.

of-sight (LOS) component is accompanied by other components due to signal diffraction and single- or multiple-signal reflections off surrounding surfaces and obstacles (e.g., the glass facade of a nearby building, poles, trees, etc.). The combination of multiple components distorts the received signal and causes errors in the pseudorange and phase measurements.

Unlike the study of ionospheric modeling errors, for application in urban mapping, multipath errors cannot be characterized with data from survey stations with a clear view of the sky. This section considers a simulation approach for scalable analysis of multipath tracking errors in an urban environment. The objective of this study was to inspect the presence of persistent biases caused by multipath due to the surrounding structure in the navigation solution averaged over multiple sessions

a) *Scenario Setup*: The present simulation study was based on the open-access Land Mobile Satellite Channel Model (LMSCM) [19], itself based on extensive experimentation with a wideband airborne transmitter at GNSS frequencies in urban and suburban environments. The simulated corridor is composed of buildings, trees, and poles.

Some of the important parameters for the generation of the scene are summarized in Table II. Multi-GNSS satellite trajectories were generated at randomly-selected times based on GPS and Galileo satellite almanac data. An average of 25 satellites were available above an elevation mask of 5° , consistent with modern multi-GNSS receivers. The satellites were assumed to be stationary over the simulation period of 60 s. Navigation solution errors were computed over 1000 60-s sessions.

TABLE II
SOME URBAN SCENARIO PARAMETERS.

Distance from road center to buildings	24 m
Distance from road center to vehicle	5 m
Mean distance between road center and trees	20 m
Antenna height	2 m
Mean building width	30 m
Building width standard deviation	25 m
Mean building height	40 m
Building height standard deviation	20 m
Probability of gap between buildings	0.5
Mean gap width	30 m
Mean distance between trees	60 m
Mean distance between poles	25 m

The vehicle trajectory was kept consistent across all 1000 driving sessions to avoid decorrelation of multipath error due to variable receiver motion. The trajectory, parametrized by its speed and heading as described in [20], is shown in Fig. 2. The 60 s long trajectory simulates a vehicle in stop-and-go traffic executing one 90° right turn. The three low-speed intervals in the simulated trajectory present severe multipath effects since multipath errors decorrelate slowly, and thus tend to reinforce one another within the navigation filter, when the vehicle moves slowly.

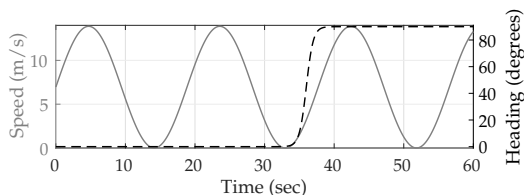


Fig. 2. Vehicle speed (solid line) and heading (dashed line) simulating stop-and-go motion with a 90° right turn.

b) Multipath Simulation: The LMSCM generates power, delay, and carrier phase for N LOS and echo signals. The interaction of the LOS with the simulated obstacles is governed by deterministic models for attenuation, diffraction, and delay. The LOS signal may be composed of more than one, say N_{LOS} , components due to signal diffraction. In the special case of an unobstructed LOS signal $N_{\text{LOS}} = 1$.

The LMSCM generates the $N - N_{\text{LOS}}$ NLOS echoes stochastically based on satellite azimuth and elevation, receiver dynamics, and general characteristics of the scene (e.g., an *urban car* scenario). This stochastic procedure might not be representative of multipath over multiple sessions through the same urban corridor, where certain echoes might persist over different sessions. To address this limitation,

the LMSCM was augmented by the present authors to generate one- and two-bounce deterministic reflective NLOS echoes off the simulated buildings, and a one-bounce NLOS echo off the ground surface, thus simulating a total of $N + 3$ signal components. Since the deterministic specular reflections are expected to be the stronger than other diffracted and multiple-bounce NLOS echoes, the amplitudes for reflective echoes were drawn from the distribution of the strongest echo generated stochastically by the LMSCM at each epoch. By experiment, this distribution was found to be log-normal with a mean of -22 dB and standard deviation of 5 dB. A random carrier-phase offset was added at the reflection point every time a new reflective echo was spawned to simulate the material-specific phase offset introduced by the reflection process.

c) Receiver: A receiver simulator was developed to account for the mediating effects that a receiver's tracking loops and navigation filter have on multipath-induced position errors in a receiver's reported position solution. If $R(\tau)$ denotes the correlation function of the GNSS signal's spreading code, then the multipath delay error in the tracked code phase, relative to unobstructed LOS, is given as the solution to [21]

$$0 = S_{\text{coh}}(\tau) \triangleq \sum_{i=0}^{N+2} A_i \cos(\theta_i - \theta_c) \times \left[R\left(\tau - \tau_i + \frac{d}{2}\right) - R\left(\tau - \tau_i - \frac{d}{2}\right) \right],$$

where A_i , θ_i , and τ_i are the amplitude, carrier phase, and excess propagation delay with respect to an unobstructed LOS signal of the i th received signal component, respectively, and θ_c is the tracked carrier-phase of the combined received signal. The parameter d is the early-to-late correlator spacing in the receiver. It is well-known that a wide-bandwidth receiver with narrow correlator spacing mitigates the effect of multipath [21]. To this end, the receiver considered in this simulation implements $d = 0.1$. It must be mentioned that $R(\tau)$ was implemented as the correlation function for GPS L1 C/A identically for all the simulated signals. Modernized GNSS signals have better multipath mitigation characteristics [8], but this behavior was not included in the simulation.

In a GNSS receiver, the phase lock loop's phase-lock indicator indicates whether a sufficiently strong LOS signal is available, enabling carrier lock [4]. To emulate similar behavior, the simulator's phase-lock indicator is asserted only if (1) the tracked Doppler frequency does not deviate significantly from a second-order polynomial, and (2) the strongest received component (either LOS or NLOS) is attenuated no more than 25 dB with respect to an unattenuated signal.

d) Navigation Filter: At each epoch, n_z multipath-free, ionosphere-free, and troposphere-free simulated pseudorange measurements were combined with corresponding simulated multipath tracking delay errors and fed to a navigation filter that estimates the receiver state. The navigation filter implemented in this paper is an extended Kalman filter (EKF) with a nearly constant velocity motion model following [22].

The standard details of the EKF are omitted for brevity.

The effect of multipath tracking on the navigation solution is strongly dependent on the receiver’s multipath rejection scheme. Two schemes are explored here. The first is a hypothetical ideal multipath rejection scheme that excludes all signals for which the LOS signal has a smaller-than-10-dB advantage over its multipath echoes. A second realistically feasible scheme implements a normalized innovation squared (NIS) test to reject multipath signals based on measurement innovations [22]. In the absence of multipath tracking errors, the NIS statistic is chi-squared distributed with n_z degrees of freedom. If the NIS statistic exceeds a chosen threshold, then the signal with the largest normalized innovation is dropped. This continues until the NIS statistic falls below the threshold or the number of remaining signals drops to a preset minimum number of required signals.

e) Simulation Results: Fig. 3 shows the mean position error in the east, north, and up directions over 1000 sessions for the two multipath rejection schemes mentioned previously. From Fig. 3a, it can be seen that sub-20 cm average error is achievable with hypothetical ideal multipath exclusion. Fig. 3b shows that the NIS test based exclusion of signals was able to approach the performance of ideal exclusion in the horizontal plane, save for the first stationary period where the vehicle was moving at low speed between buildings on both sides. The average vertical position error was much worse, growing as large as 1.75 m in magnitude.

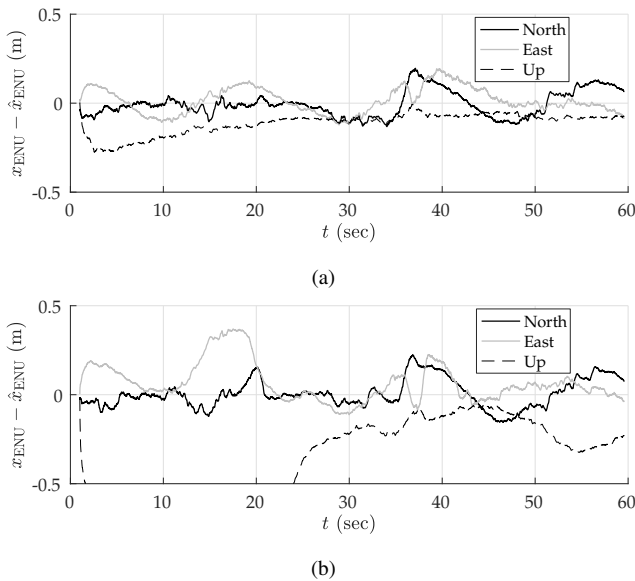


Fig. 3. Mean position error in the east-north-up (ENU) frame over 1000 sessions due to multipath. (a) Ideal multipath exclusion. (b) NIS-based multipath exclusion. The black, gray, and dashed-black lines represent the error in the east, north, and up directions, respectively. The up error in the bottom panel reached a maximum magnitude of 1.75 m.

Table III shows the 95-percentile horizontal error magnitude for increasing averaging ensemble sizes and for both ideal and NIS-based multipath exclusion. To compute the 95-percentile horizontal error for an averaging ensemble size N , first the 1000 simulated sessions are randomly grouped in to $1000/N$ disjoint ensembles of size N each. The horizontal

position errors are then averaged for each group, and the 95-percentile error is computed from the $1000/N$ data points.

The 0–60 s average case lists the 95-percentile error over the entire trajectory, whereas the 13–19 s average case lists the 95-percentile error in the worst-case segment of the trajectory in terms of horizontal position bias and standard deviation. This challenging segment is illustrative of persistent problem spots that will arise in urban areas, within which multipath-induced biases will be larger than average. As expected, the 95-percentile error in Table III shrank as the averaging ensemble size became larger. For the urban corridor and vehicle dynamics considered in this simulation, NIS-based exclusion achieved 35 cm 95-percentile horizontal error with averaging over 100 sessions. Even in the worst-case region of the trajectory, the 95-percentile horizontal error remained below 50 cm. As multipath exclusion approaches the ideal case, with aid from other sensors or a 3D model of the surroundings, for example, the 95-percentile horizontal error could be reduced to as low as 25 cm for the simulated corridor.

TABLE III
95-PERCENTILE HORIZONTAL ERRORS.

Averaging Ensemble Size:		1	16	50	100
Ideal	0–60 s average (m)	1.5910	0.4078	0.2696	0.2147
	13–19 s average (m)	2.5925	0.6416	0.3544	0.2609
NIS	0–60 s average (m)	1.7851	0.5169	0.3920	0.3526
	13–19 s average (m)	3.1217	0.8456	0.5950	0.4702

From the Section III-C.3’s analysis of asymptotic ionospheric errors, and from this section’s multipath simulation study, one can draw the following conclusion: so long as the asymptotic horizontal position errors of the ionosphere corrections are below 5 cm, as is true for the Fast-PPP model, and assuming statistical independence of ionospheric and multipath errors, it appears feasible to achieve 50-cm horizontal positioning accuracy at approximately 95% in moderately urban environments by averaging over 100 mapping sessions.

IV. EMPIRICAL RESULTS

To validate the results obtained in the above analyses, GNSS data were collected in a moderate urban area north of the University of Texas at Austin campus in Austin, TX. This section presents the data collection setup and error statistics of various flavors of code-phase GNSS positioning.

A. Rover and Reference Platforms

The rover GNSS receiver was fed by two Antcom G8Ant-3A4TNB1 triple-frequency patch antennas separated by just over one meter, whose signals were routed to a unified RF front end. The experimental setup also included a surveyed GNSS reference station that aids in the generation of the ground truth trajectory.

The intermediate frequency (IF) GNSS data were processed by a software-defined GNSS receiver tracking signals from GPS L1 C/A, GPS L2CLM, Galileo E1, and SBAS.

Data from both GNSS antennas were used to reconstruct a sub-dm-accurate CDGNSS-based ground truth trajectory, as described in [4]. Enhanced code-phase positioning was performed on the data from the primary antenna, incorporating precise orbit and clock products from IGS, ionospheric corrections from WAAS satellites, and the Saastamoinen model for tropospheric corrections, in addition to NIS-based exclusion of multipath signals. Double-differenced pseudorange-based positioning was also performed with the data from the primary antenna, as discussed later in this section. The code-phase-based position estimates were compared against the ground truth from the primary antenna to study the code-phase positioning error statistics.

B. Test Route

The test route was a 1-km loop north of the University of Texas at Austin campus. The route included a variety of light-to-moderate urban conditions, from open-sky to overhanging trees to built-up areas. The Dean Keeton corridor, toward the left in Fig. 4, was the most challenging stretch along the test route for GNSS positioning. It passes below a pedestrian bridge and is flanked on both sides by buildings ranging from 30 to 65 meters tall set back 28 meters from the center of the roadway.



Fig. 4. An overview of the 1-km test route. The Dean Keeton corridor, toward the left, is spanned by a pedestrian bridge and flanked by buildings on both sides.

To study the code-phase-based positioning error characteristics over time-separated sessions in the same area, multiple laps of the test route were driven over six separate campaigns. The following GNSS error charts are presented for a total of 75 laps of the test route.

C. Empirical GNSS Error Analysis

Fig. 5 shows the error in the enhanced code-phase GNSS position solutions with respect to the ground truth. The error is plotted versus the distance along the 1-km loop. The beginning of this loop was taken to be immediately after the overhead pedestrian bridge along the Dean Keeton corridor. It is observed that the enhanced code-phase GNSS errors are clustered separately for each of the campaigns, and that each cluster is offset from zero by as much as 1 m in the horizontal plane. Such error characteristics are representative of ionospheric modeling errors, which have a long decorrelation time. It is also evident that the error

variance was larger as the receiver exits the challenging portion of the loop at which point the tracking loops were recovering from signal loss under the bridge. The effect was especially pronounced in the vertical direction.

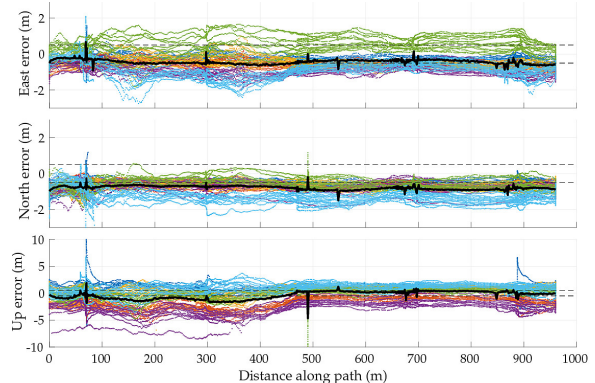


Fig. 5. Errors in enhanced code-phase position estimates with respect to ground truth in the east, north, and up directions. Different colors distinguish data from six different campaigns. The dashed reference lines are drawn at ± 50 cm. The solid black lines show the mean positioning error over the six campaigns.

On the basis of Fig. 5, one might be tempted to conclude that errors in enhanced code-phase and stand-alone GNSS navigation solutions are substantially non-zero-mean, especially in the north and up directions, despite the overhead GNSS constellation changing substantially between sessions. It certainly appears that the permanent structures (buildings, bridge) along the test loop left a bias in the vertical direction during the first 400 m along the loop. However, the bias in the north direction, and to a lesser extent in the east, may only be an artifact of the small sample size: ionospheric modeling errors were not yet averaged down to nearly zero in the east and ~ 30 cm in the north, as one would expect from the WAAS ionospheric model (see Table I).

Given that the asymptotic properties of ionospheric modeling errors are better understood than those of multipath errors, it is instructive to eliminate, insofar as possible, all ionospheric modeling errors from the along-track error histories. To this end, a differential code phase GNSS technique was applied whereby the navigation solution was based on double-difference pseudorange measurements using data from a nearby reference station at an accurately known location. Such double differencing over a short 1-km baseline eliminates virtually all ionospheric and tropospheric errors, but does nothing to reduce vehicle-side multipath. Thus, one can empirically examine multipath effects in isolation from ionospheric effects.

Fig. 6 shows the results of this study based on all six data capture campaigns. Note that biases for all components are much smaller. It appears that for the test route chosen, non-zero-mean horizontal errors in the enhanced code phase positions were almost entirely driven by ionospheric modeling errors, and not by persistent effects of multipath due to the permanent structures along the test route. This is broadly consistent with the analyses presented earlier in

this paper on position-domain biases due to ionospheric and multipath errors. However, it does appear that a bias due to multipath remained in the vertical direction over the first 400 m, even when ionospheric errors were removed. Apparently, the arrangement of buildings over this segment caused non-line-of-sight effects that did not average away. Mercifully, horizontal errors, which appear to be close to zero-mean over the six campaigns, matter most for high-accuracy digital mapping, since obstacle avoidance and vehicle coordination are largely 2-D problems.

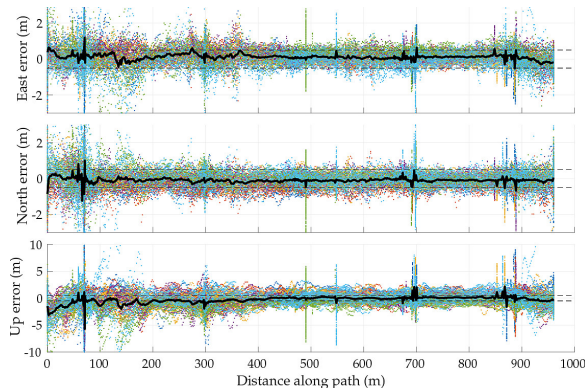


Fig. 6. Errors in double-differenced pseudorange-based position estimates with respect to ground truth in the east, north, and up directions. Different colors distinguish data from six different campaigns. Dashed reference lines are drawn at ± 50 cm. The solid black lines show the mean positioning error over the six campaigns.

Based on Fig. 6, one can conclude that multi-session averaging with a sufficiently accurate ionospheric model, such as the Fast PPP model, yields sub-50-cm global referencing accuracy for digital maps in moderately urban environments in the horizontal plane with code-phase-based GNSS, even in the presence of persistent multipath.

V. CONCLUSIONS

The accuracy limits of collaborative global referencing of digital maps with standard GNSS were explored through simulation and real data. The asymptotic average of position errors due to thermal noise, satellite orbit and clock errors, and tropospheric modeling errors were assumed to be negligible. It has been shown that the position error due to inaccurate ionospheric modeling may lead to persistent dm-level biases in the horizontal position if the corrections are sourced from the IGS GIM, but other recent models such as the Fast PPP IONEX GIM perform better in this regard. Multipath errors persist with multiple mapping sessions through the same urban corridor and may not be zero mean. With adequate multipath exclusion, persistent multipath biases may be reduced below 50 cm on average. In conclusion, sub-50-cm accurate digital mapping has been shown to be feasible in moderately urban environments in the horizontal plane after multiple mapping sessions with code-phase-based GNSS, but larger biases persist in the vertical direction.

REFERENCES

- [1] H. Wymeersch, G. Seco-Granados, G. Destino, D. Dardari, and F. Tufvesson, "5G mmWave positioning for vehicular networks," *IEEE Wireless Communications*, vol. 24, no. 6, pp. 80–86, 2017.
- [2] J. Levinson, M. Montemerlo, and S. Thrun, "Map-based precision vehicle localization in urban environments," in *Robotics: Science and Systems*, vol. 4. Citeseer, 2007, p. 1.
- [3] J. Levinson and S. Thrun, "Robust vehicle localization in urban environments using probabilistic maps," in *Robotics and Automation (ICRA), 2010 IEEE International Conference on*. IEEE, 2010, pp. 4372–4378.
- [4] T. E. Humphreys, M. Murrian, and L. Narula, "Low-cost precise vehicular positioning in urban environments," in *2018 IEEE/ION Position, Location and Navigation Symposium (PLANS)*, April 2018, pp. 456–471.
- [5] J. J. Hutton, N. Gopaul, X. Zhang, J. Wang, V. Menon, D. Rieck, A. Kipka, and F. Pastor, "Centimeter-level, robust GNSS-aided inertial post-processing for mobile mapping without local reference stations," vol. XLI-B3. Gottingen: Copernicus GmbH, 2016, pp. 819–826.
- [6] S. Rogers, "Creating and evaluating highly accurate maps with probe vehicles," in *Intelligent Transportation Systems, 2000. Proceedings. 2000 IEEE*. IEEE, 2000, pp. 125–130.
- [7] V. L. Knoop, P. F. de Bakker, C. C. Tiberius, and B. van Arem, "Lane determination with GPS precise point positioning," *IEEE Transactions on Intelligent Transportation Systems*, vol. 18, no. 9, pp. 2503–2513, 2017.
- [8] M.-S. Circiu, M. Meurer, M. Felix, D. Gerbeth, S. Thörlert, M. Vergara, C. Enneking, M. Sgammini, S. Pullen, and F. Antreich, "Evaluation of GPS L5 and Galileo E1 and E5a performance for future multifrequency and multiconstellation GBAS," *Navigation*, vol. 64, no. 1, pp. 149–163, 2017.
- [9] P. Xie and M. G. Petovello, "Measuring GNSS multipath distributions in urban canyon environments," *IEEE Transactions on Instrumentation and Measurement*, vol. 64, no. 2, pp. 366–377, 2015.
- [10] A. Rovira-Garcia, J. Juan, J. Sanz, G. González-Casado, and D. Ibáñez, "Accuracy of ionospheric models used in GNSS and SBAS: methodology and analysis," *Journal of geodesy*, vol. 90, no. 3, pp. 229–240, 2016.
- [11] J. Böhm, G. Möller, M. Schindelegger, G. Pain, and R. Weber, "Development of an improved empirical model for slant delays in the troposphere (GPT2w)," *GPS Solutions*, vol. 19, no. 3, pp. 433–441, 2015.
- [12] L. Narula, J. M. Wooten, M. J. Murrian, D. M. LaChapelle, and T. E. Humphreys, "Accurate collaborative globally-referenced digital mapping with standard GNSS," *Sensors*, vol. 18, no. 8, 2018. [Online]. Available: <http://www.mdpi.com/1424-8220/18/8/2452>
- [13] M. J. Murrian, C. W. Gonzalez, T. E. Humphreys, K. M. P. Jr., D. P. Shepard, and A. J. Kerns, "Low-cost precise positioning for automated vehicles," *GPS World*, vol. 27, no. 9, pp. 32–39, September 2016.
- [14] P. Misra and P. Enge, *Global Positioning System: Signals, Measurements, and Performance*, revised second ed. Lincoln, Massachusetts: Ganga-Jumana Press, 2012.
- [15] "GPS satellite ephemerides / satellite & station clocks," <http://www.igs.org/products>, accessed: 2018-03-30.
- [16] A. Rovira-Garcia, J. M. Juan, J. Sanz, and G. González-Casado, "A worldwide ionospheric model for fast precise point positioning," *IEEE Transactions on Geoscience and Remote Sensing*, vol. 53, no. 8, pp. 4596–4604, Aug 2015.
- [17] J. Boehm, B. Werl, and H. Schuh, "Troposphere mapping functions for GPS and very long baseline interferometry from European Centre for Medium-Range Weather Forecasts operational analysis data," *Journal of Geophysical Research: Solid Earth*, vol. 111, no. B2, 2006.
- [18] J. Böhm, A. Niell, P. Tregoning, and H. Schuh, "Global mapping function (GMF): A new empirical mapping function based on numerical weather model data," *Geophysical Research Letters*, vol. 33, no. 7, 2006.
- [19] A. Lehner and A. Steingass, "A novel channel model for land mobile satellite navigation," in *Proceedings of the ION GNSS Meeting*, 2005, pp. 13–16.
- [20] —, "Technical note on the Land Mobile Satellite Channel Model - Interface Control Document," May 2008.
- [21] M. S. Braasch, *Springer Handbook of Global Navigation Satellite Systems*. Springer, 2017, ch. Multipath, pp. 443–468.

- [22] Y. Bar-Shalom, X. R. Li, and T. Kirubarajan, *Estimation with Applications to Tracking and Navigation*. New York: John Wiley and Sons, 2001.